

# Three-Dimensional, Transient Model for Laser Machining of Ablating/Decomposing Materials

Michael F. Modest\*  
The Pennsylvania State University  
University Park, Pennsylvania

## Abstract

A three-dimensional conduction model has been developed to predict the transient temperature distribution inside a thick solid that is irradiated by a moving laser source, and the changing shape of a groove carved into it by evaporation of material. The laser may operate in CW or in pulsed mode with arbitrary temporal as well as spatial intensity distribution. The governing equations are solved using a finite difference method on an algebraically-generated boundary-fitted coordinate system. The accuracy of the present transient model was verified by comparison with previous three-dimensional codes that were limited to quasi-steady CW operation. Groove shapes and temperature distributions, as well as their transient development, for various machining conditions are presented, demonstrating the differences in the ablation process between CW, pulsed and Q-switched (or other pulses of extremely short duration) laser operation.

## Nomenclature

|              |  |
|--------------|--|
| $c$          | specific heat  |
| $C_1, C_2$   | constants in Arrhenius relation  |
| $\mathbf{F}$ | irradiation flux vector  |
| $F_0$        | radiation flux density at center of beam at focal plane                  |
| $f$          | functional variation of thermal diffusivity, $= \alpha_H/\alpha_{H,ref}$ |

---

\*Professor, Department of Mechanical Engineering

|  |  |
|--|--|
| $\Delta h_{re}$  | “heat of removal”  |
| $\hat{\mathbf{i}}, \hat{\mathbf{j}}, \hat{\mathbf{k}}$ | unit vector in $x$ , $y$ and $z$ directions                          |
| $J$  | Jacobian of transformation   |
| $k$  | thermal conductivity   |
| $\dot{m}''$  | mass rate of ablation per unit area                                  |
| $\hat{\mathbf{n}}$                                     | unit surface normal  |
| $N_k, N_k^*$   | conduction-to-laser power parameters                                 |
| $N_\xi, N_\eta, N_\zeta$                               | number of grid points in $\xi$ , $\eta$ and $\zeta$ directions       |
| $\mathbf{Q}$   | dimensionless irradiation flux vector at surface, = $\mathbf{F}/F_0$ |
| $\bar{s}(\bar{x}, \bar{y})$                            | local groove depth   |
| $s(x, y)$  | dimensionless groove depth   |
| $Ste, Ste^*$   | Stefan numbers (ablation energy-to-sensible heat parameters)         |
| $\bar{t}$  | time   |
| $t$  | dimensionless time   |
| $T$  | temperature  |
| $u$  | laser scanning speed   |
| $U$  | laser speed-to-diffusion speed parameter                             |
| $v_n$  | ablation velocity (of solid surface), = $\dot{m}''/\rho$             |
| $w, w_0$   | $1/e^2$ radius of laser beam (at focal plane)                        |
| $W$  | dimensionless radius of laser beam, = $w/w_0$                        |
| $\bar{x}, \bar{y}, \bar{z}$                            | Cartesian coordinates  |
| $x, y, z$  | dimensionless Cartesian coordinates                                  |

### Greek letters

|                    |  |
|--------------------|--|
| $\alpha_H$         | thermal diffusivity                              |
| $\alpha$           | local effective absorptivity at laser wavelength |
| $\beta_\infty$     | far-field beam divergence                        |
| $\lambda$          | wavelength of laser radiation                    |
| $\lambda_k$        | conductivity correction factor                   |
| $\rho$             | density of the medium                            |
| $\delta$           | difference operator                              |
| $\theta$           | dimensionless temperature                        |
| $\xi, \eta, \zeta$ | dimensionless computational coordinates          |

## Subscripts

|                    |   |
|--------------------|---|
| $r_e$              | evaluated at evaporation (or decomposition) temperature |
| $\xi, \eta, \zeta$ | derivative with respect to this variable                |
| 0                  | at focal plane  |
| $\infty$           | evaluated at ambient conditions, or located far away    |

## 1 Introduction

Since their invention in 1960, lasers have found diverse applications in engineering and industry because of their ability to produce high-power beams. Laser applications include welding, drilling, cutting, scribing, machining, heat treatment, medical surgery, and others.

One of the principle advantages of laser cutting is its ability to cut very hard materials easily. Ceramics are among the most difficult materials to machine by conventional machining techniques, since they are very hard and brittle. The cost of machining ceramics into complex shapes is often prohibitive if conventional machining is used. Lasers may provide a cheaper alternative to conventional machining and have found wide-spread use in industry. However, the physical phenomena involved in many laser applications are not fully understood. A better quantitative understanding of the physical mechanisms governing these phenomena will diminish the need for extensive trial and error experiments, needed to use lasers for complex machining operations on newly developed materials.

Modeling of laser drilling, cutting and scribing has been addressed by a number of investigators. Simple one-dimensional drilling models have been given by Dabby and Paek [1] and Wagner [2]. Other approximate laser drilling models have been developed by Schuöcker and Abel [3], Petring *et al.* [4], and others. Laser scribing, drilling and cutting of ablating and/or decomposing materials has been investigated primarily by Modest and coworkers. They developed a number of models [5–16], ranging from quasi-onedimensional to fully three-dimensional models. The reader is referred to these papers for a complete description of their various aims and capabilities, as well as to a monograph by Chryssolouris [17] for a review of other pertinent theoretical work that has dealt with the different aspects of material removal with lasers.

All theoretical models to date have dealt only with quasi-steady material removal by a CW

(continuous wave) laser. In the present paper the three-dimensional finite-difference model on a boundary-fitted coordinate system of Roy and Modest [13] will be revamped and augmented to allow the treatment of transient effects, such as start-up and shut-down effects, as well as pulsed laser operation. Very short pulses, such as 100ns pulses from a Q-switched Nd-YAG laser, with long off-times as long as 1ms (or a laser-on-time fraction of  $10^{-4}$ ) will be considered, as well as very long pulses, such as pulses of several ms duration from a CO<sub>2</sub> laser with large laser-on-time fraction.

## 2 Theoretical Background

In order to obtain a realistic yet feasible description of the evaporation front in a moving solid subjected to a concentrated laser beam, the following simplifying assumptions similar to Roy and Modest [13] will be made:

1. The solid moves with constant velocity  $u$ .
2. The solid is isotropic.
3. Density variations of the solid with temperature are negligible.
4. The material is opaque, *i.e.*, the laser beam does not penetrate appreciably into the medium. This assumption may be somewhat questionable even for materials with large absorption coefficient, if the laser beam radius is very small (say,  $< 10 \mu\text{m}$ ) and/or the pulse duration is very short (say,  $< 100 \text{ns}$ ) resulting in very shallow heat-affected zones (a few  $\mu\text{m}$  or less).
5. Change of phase from solid to vapor (or decomposition products) occurs in a single step with a rate governed by a simple Arrhenius relation. Real materials may display significantly different behavior as discussed by Roy and Modest [13]. Such effects are included by employing the total amount of energy required to remove material, referred to as “heat of removal”,  $\Delta h_{\text{re}}$ .
6. The evaporated material does not interfere with the incoming laser beam and ionization of the gas does not occur, which is true for most cutting and drilling applications at moderate power levels. The gas is transparent and there are no droplets and particles (or they are removed by an external gas jet).
7. Heat losses by convection and radiation are negligible as compared to the intensity of the incident beam (Modest and Abakians, [6]).

8. Multiple reflections of laser radiation within the groove are neglected. This is a limitation which restricts the present model to shallow grooves or materials with high absorptivities (even at grazing angles), *e.g.*, if the evaporation surface is rough. Multiple reflections of laser radiation within the groove have been addressed by Bang and Modest [14–16].

In previous work of the author the coordinate system has been affixed to the laser, *i.e.*, the laser position remains stationary and the material moves relative to it with constant velocity  $u$ . For quasi-steady operation of a CW laser machining process this results in a quasi-steady groove geometry (not a function of time in that coordinate system). Therefore, once determined, nodal points for the numerical scheme do not move with time. If simple transient effects, such as laser turn-on, are considered, nodal positions will change as the surface recedes until quasi-steady state is reached; this nodal movement, while undesirable from the view point of numerical stability, cannot be avoided no matter where the coordinate origin is placed. In the case of pulsed laser operation, shortly after the beginning of the pulse the surface recedes, similar to the turn-on effects of a CW laser. Once the laser pulse has ended ablation ceases almost instantly. However, if the origin is fixed to the laser, the nodes in the material keep moving (relative to the laser position) and must be constantly recalculated (resulting in accumulation of errors for the description of the surface). Therefore, to describe the operation of pulsed lasers it is advantageous to fix the coordinate system to the ablating material, letting the laser scan across the body. (However, the formation of a quasi-steady groove geometry is not possible with this coordinate system). Under these conditions the transient heat transfer equation for a large, thick solid irradiated by a Gaussian laser beam that moves with constant velocity  $u$  into the positive  $\bar{x}$ -direction (see Fig. 1) may be expressed in terms of temperature  $T$  as:

$$\rho c \frac{\partial T}{\partial t} = \bar{\nabla} \cdot (k \bar{\nabla} T), \quad (1)$$

(where  $\bar{\nabla}$  denotes a gradient with respect to dimensional  $\bar{x}, \bar{y}, \bar{z}$  coordinates) subject to the boundary conditions,

$$\bar{x} \rightarrow \pm\infty, \quad \bar{y} \rightarrow \pm\infty, \quad \bar{z} \rightarrow +\infty : \quad T = T_\infty \quad (2a)$$

$$\bar{z} = \bar{s}(\bar{x}, \bar{y}) : \quad \alpha \mathbf{F} \cdot \hat{\mathbf{n}} = -\hat{\mathbf{n}} \cdot (k \bar{\nabla} T) + v_n \rho \Delta h_{re} \quad (2b)$$

and an appropriate initial condition, such as

$$\begin{aligned} \bar{t} = 0 : \quad T(\bar{x}, \bar{y}, \bar{z}, 0) &= T_\infty, \\ \bar{s}(\bar{x}, \bar{y}, 0) &= 0. \end{aligned} \quad (2c)$$

Boundary condition (2b) states that the irradiation absorbed at the top surface is used up by conduction losses into the solid and by evaporation, if present (if no evaporation takes place, *i.e.*, during warm-up, cool-down and in regions too far away sideways from the laser beam, the surface recession velocity vanishes, *i.e.*,  $v_n = 0$ ).

The energy intensity distribution,  $\mathbf{F}$ , for a focussed Gaussian laser beam having a waist  $w_0$  at the focal plane  $z_0$  is given by Kogelnik and Li [18], and for a laser moving with constant velocity  $u$  into the positive  $\bar{x}$  direction is:

$$\mathbf{F} = \frac{w_0^2}{w^2} F_0 \phi(\bar{t}) e^{-2[(\bar{x}-u\bar{t})^2+\bar{y}^2]/w^2(\bar{z})} \frac{\hat{\mathbf{s}}}{\hat{\mathbf{s}} \cdot \hat{\mathbf{k}}}, \quad (3a)$$

where

$$w^2(\bar{z}) = w_0^2 + \beta_\infty^2 (\bar{z} - \bar{z}_0)^2, \quad (3b)$$

defines the beam radius,  $w$ , away from focus and

$$\beta_\infty = \frac{\lambda}{\pi w_0} \quad (3c)$$

is the far-field beam divergence angle for the diffraction-limited case of a Gaussian beam. Also  $F_0 = 2P/\pi w_0^2$  is the flux at the center of a Gaussian beam at the focal plane,  $P$  is the total laser power, and  $w_0$  is the  $1/e^2$ -radius of the focal spot containing 86.5% of the beam's energy. If the laser beam is visualized as consisting of a bundle of rays into the direction  $\hat{\mathbf{s}}(\bar{x}, \bar{y}, \bar{z})$ , perpendicular to the wave-front of propagation, then  $\hat{\mathbf{s}}$  can be related to the radius of the wave-front [19],  $\bar{r}_c(z)$ , as:

$$\frac{\hat{\mathbf{s}}}{\hat{\mathbf{s}} \cdot \hat{\mathbf{k}}} = \frac{\bar{x}\hat{\mathbf{i}} + \bar{y}\hat{\mathbf{j}}}{\sqrt{\bar{r}_c^2(\bar{z}) - \bar{x}^2 - \bar{y}^2}} + \hat{\mathbf{k}}, \quad (4a)$$

$$\bar{r}_c(z) = (\bar{z} - \bar{z}_0) \left[ 1 + \frac{w_0^2/\beta_\infty^2}{(\bar{z} - \bar{z}_0)^2} \right]. \quad (4b)$$

Results given in this paper are limited to the Gaussian laser described above to simplify their presentation; arbitrary spatial intensity profiles are readily incorporated.

Finally,  $\phi(\bar{t})$  defines the temporal intensity variation during a laser pulse period of duration  $\bar{t}_p = \bar{t}_{p,\text{on}} + \bar{t}_{p,\text{off}}$ , and is normalized such that

$$\frac{1}{\bar{t}_p} \int_{\bar{t}}^{\bar{t}+\bar{t}_p} \phi(\bar{t}) d\bar{t} = 1. \quad (5)$$

Therefore, for a CW laser  $\phi \equiv 1$ .

Boundary conditions (2) are sufficient to solve equation (1) for the temperature if the groove shape  $\bar{s}$  is already established ( $v_n = 0$ ) or if  $v_n$  is otherwise known. We will assume in this paper that the ablation and/or decomposition of the solid material is governed by a simple reaction equation of the Arrhenius type, similar to the equilibrium evaporation rate equation originally developed by Langmuir and given, *e.g.*, in Wei and Ho [20]. With such a reaction equation the rate of mass loss per unit area is described by

$$\dot{m}'' = \rho v_n = \rho \bar{C}_1 e^{C_2(1-T_{re}/T)}; \quad C_2 = \frac{\Delta h_{re}}{RT_{re}}, \quad (6)$$

where  $T_{re}$  is the equilibrium ablation (or ‘‘removal’’) temperature,  $R$  is the gas constant of the ablated vapor, and  $\bar{C}_1$  is a preexponential factor, which may depend on temperature. Clearly, if  $C_2 \gg 0$ , no ablation/decomposition occurs as long as  $T < T_{re}$ . Once  $T$  gets close to  $T_{re}$  the material rapidly recedes, using up a lot of laser energy, so that  $T$  can exceed  $T_{re}$  by only a very small amount. This formulation has the further advantage that – if decomposition energy data are not available, as is the case for most relevant materials – choosing a large value for  $C_2$  ( $\simeq 100$ -500) forces single-temperature ablation at  $T \simeq T_{re}$ .

To non-dimensionalize the governing equations and boundary conditions the following non-dimensional variables and parameters are introduced (Roy and Modest [13]):

$$\begin{aligned} x = \bar{x}/w_0; \quad y = \bar{y}/w_0; \quad z = \bar{z}/w_0; \quad s = \bar{s}/w_0; \quad t = \alpha_{H,re} \bar{t}/w_0^2; \quad \theta = \frac{\int_{T_\infty}^T k dT}{\int_{T_\infty}^{T_{re}} k dT}; \\ U = \frac{uw_0}{\alpha_{H,re}}; \quad V_n = \frac{v_n w_0}{\alpha_{H,re}}; \quad N_k = \frac{k_{re}(T_{re} - T_\infty)}{F_0 w_0}; \quad Ste = \frac{\Delta h_{re}}{c_{re}(T_{re} - T_\infty)}; \quad (7) \\ f = \alpha_H/\alpha_{H,re}; \quad \lambda_k = \frac{\int_{T_\infty}^{T_{re}} k dT}{k_{re}(T_{re} - T_\infty)}; \quad N_k^* = N_k \lambda_k; \quad Ste^* = Ste/\lambda_k. \end{aligned}$$

Physically,  $N_k$  approximates the ratio of conduction losses, for a surface normal to irradiation, and the absorbed laser flux;  $Ste$  is the Stefan number that compares ablation energy with sensible heat,  $\lambda_k$  is a conductivity correction factor (to accommodate variable properties),  $U$  relates the laser scanning speed to that of thermal diffusion into the medium, and  $V_n$  represents a similar non-dimensional transient recession of the evaporating surface with respect to the laser. The function  $f$  describes the variable thermal diffusivity. The factor  $\sqrt{2}$  that appeared in some of the dimensionless groups of Roy and Modest [13] has been omitted in order to be consistent with work

of other authors. Also, for convenience, the Kirchhoff transformation (Carslaw and Jaeger, [21]) is used to non-dimensionalize temperature. The non-dimensional form of the governing equation then follows as:

$$\frac{1}{f} \frac{\partial \theta}{\partial t} = \nabla^2 \theta, \quad (8)$$

where gradients are now with respect to dimensionless coordinates, and the boundary conditions become:

$$x \rightarrow \pm \infty, \quad y \rightarrow \pm \infty, \quad z \rightarrow +\infty : \quad \theta = 0; \quad (9a)$$

$$z = s(x, y) : \quad \alpha \mathbf{Q} \cdot \hat{\mathbf{n}} = -N_k^* [\hat{\mathbf{n}} \cdot \nabla \theta - V_n \text{Ste}^*];$$

$$\mathbf{Q} = \frac{\mathbf{F}}{F_0} = \frac{\phi(t)}{W^2} \exp \left[ -2 \frac{(x - Ut)^2 + y^2}{W^2} \right] \frac{\hat{\mathbf{s}}}{\hat{\mathbf{s}} \cdot \hat{\mathbf{k}}},$$

$$W^2(z) = 1 + \beta_\infty^2 (z - z_0)^2; \quad (9b)$$

$$z = s(x, y) : \quad V_n = C_1 e^{C_2 [1 - T_{re}/T(\theta)]}, \quad C_1 = \bar{C}_1 w_0 / \alpha_{H,re}. \quad (9c)$$

Equation (8) with its boundary conditions (9) forms a complete set of dimensionless equations in transient form for the solution of the groove shape  $s(x, y, t)$  and temperature field  $\theta(x, y, z, t)$ . This set of equations is similar to the one used previously (Roy and Modest [13]) except that the definitions of some dimensionless terms have been modified, a new ablation model is used (a more general Arrhenius reaction rate as opposed to fixed-temperature ablation), and transient effects are included.

### 3 Solution Approach

The accuracy of a numerical finite difference solution of the governing equation with its non-linear boundary conditions applied to a complex groove geometry is strongly affected by the choice of nodal placement as well as the coordinate system in which the equations are cast. The boundary-fitted coordinate system is useful to this problem in two ways: Body-conforming grids simplify the application of boundary conditions since grid lines coincide with the boundary of the body; secondly, curvilinear grids may be clustered in regions of rapid change to improve solution accuracy.

### 3.1 Coordinate Transformation

The physical domain,  $(x, y, z)$ , will be transformed to a uniformly spaced rectangular coordinate region,  $(\xi, \eta, \zeta)$ . Symbolically, the functional relations are:

$$\begin{aligned} x &= x(\xi, \eta, \zeta, \tau), & y &= y(\xi, \eta, \zeta, \tau), & z &= z(\xi, \eta, \zeta, \tau), & t &= \tau; \\ \xi &= \xi(x, y, z, t), & \eta &= \eta(x, y, z, t), & \zeta &= \zeta(x, y, z, t), & \tau &= t. \end{aligned} \quad (10)$$

The functional form of the metric quantities ( $\xi_x = \partial\xi/\partial x$ ,  $\xi_y = \partial\xi/\partial y$ ,  $\xi_z = \partial\xi/\partial z$ , etc.), required to transform an equation from a physical coordinate system to computational coordinates has been given by several authors, *e.g.*, Thompson, Warsi and Mastin [22], Anderson, Tannehill and Pletcher [23], and is repeated here for convenience:

$$\frac{\partial(x, y, z)}{\partial(\xi, \eta, \zeta)} = 1/J = x_\xi(y_\eta z_\zeta - y_\zeta z_\eta) + x_\eta(y_\zeta z_\xi - y_\xi z_\zeta) + x_\zeta(y_\xi z_\eta - y_\eta z_\xi); \quad (11a)$$

$$\begin{bmatrix} \xi_x & \xi_y & \xi_z \\ \eta_x & \eta_y & \eta_z \\ \zeta_x & \zeta_y & \zeta_z \end{bmatrix} = J \begin{bmatrix} (y_\eta z_\zeta - y_\zeta z_\eta) & (z_\eta x_\zeta - z_\zeta x_\eta) & (x_\eta y_\zeta - x_\zeta y_\eta) \\ (y_\zeta z_\xi - y_\xi z_\zeta) & (z_\zeta x_\xi - z_\xi x_\zeta) & (x_\zeta y_\xi - x_\xi y_\zeta) \\ (y_\xi z_\eta - y_\eta z_\xi) & (z_\xi x_\eta - z_\eta x_\xi) & (x_\xi y_\eta - x_\eta y_\xi) \end{bmatrix}; \quad (11b)$$

$$\begin{aligned} \xi_t &= -x_\tau \xi_x - y_\tau \xi_y - z_\tau \xi_z, \\ \eta_t &= -x_\tau \eta_x - y_\tau \eta_y - z_\tau \eta_z, \\ \zeta_t &= -x_\tau \zeta_x - y_\tau \zeta_y - z_\tau \zeta_z. \end{aligned} \quad (11c)$$

The mapping functions (10) need not be known analytically; the partial derivatives  $x_\xi, x_\eta, x_\zeta$  are computed by central difference formulae, from which the metric quantities can be obtained.

### 3.2 Transformed Equations

The governing equation is transformed to the rectangular computational coordinate region. The non-conservative form of the transformed equation is easily derived as given by Thompson, Warsi and Mastin [22]:

$$\begin{aligned} \frac{1}{f} [\theta_\tau + \xi_t \theta_\xi + \eta_t \theta_\eta + \zeta_t \theta_\zeta] &= A^{\xi\xi} \theta_{\xi\xi} + A^{\eta\eta} \theta_{\eta\eta} + A^{\zeta\zeta} \theta_{\zeta\zeta} + 2A^{\xi\eta} \theta_{\xi\eta} \\ &+ 2A^{\xi\zeta} \theta_{\xi\zeta} + 2A^{\eta\zeta} \theta_{\eta\zeta} + \nabla^2 \xi \theta_\xi + \nabla^2 \eta \theta_\eta + \nabla^2 \zeta \theta_\zeta, \end{aligned} \quad (12)$$

where

$$A^{\xi\xi} = \nabla \xi \cdot \nabla \xi, \quad A^{\eta\eta} = \nabla \eta \cdot \nabla \eta, \quad A^{\zeta\zeta} = \nabla \zeta \cdot \nabla \zeta,$$

$$\begin{aligned}
A^{\xi\eta} &= \nabla\xi \cdot \nabla\eta, & A^{\xi\zeta} &= \nabla\xi \cdot \nabla\zeta, & A^{\eta\zeta} &= \nabla\eta \cdot \nabla\zeta; \\
\nabla^2\xi &= -\nabla\xi \cdot \mathbf{D}, & \nabla^2\eta &= -\nabla\eta \cdot \mathbf{D}, & \nabla^2\zeta &= -\nabla\zeta \cdot \mathbf{D}; \\
\mathbf{D} &= D^x\hat{\mathbf{i}} + D^y\hat{\mathbf{j}} + D^z\hat{\mathbf{k}}, \\
D^x &= A^{\xi\xi}x_{\xi\xi} + A^{\eta\eta}x_{\eta\eta} + A^{\zeta\zeta}x_{\zeta\zeta} + A^{\xi\eta}2x_{\xi\eta} + A^{\xi\zeta}2x_{\xi\zeta} + A^{\eta\zeta}2x_{\eta\zeta}, \\
D^y &= A^{\xi\xi}y_{\xi\xi} + A^{\eta\eta}y_{\eta\eta} + A^{\zeta\zeta}y_{\zeta\zeta} + A^{\xi\eta}2y_{\xi\eta} + A^{\xi\zeta}2y_{\xi\zeta} + A^{\eta\zeta}2y_{\eta\zeta}, \\
D^z &= A^{\xi\xi}z_{\xi\xi} + A^{\eta\eta}z_{\eta\eta} + A^{\zeta\zeta}z_{\zeta\zeta} + A^{\xi\eta}2z_{\xi\eta} + A^{\xi\zeta}2z_{\xi\zeta} + A^{\eta\zeta}2z_{\eta\zeta}.
\end{aligned}$$

The irradiation boundary condition is also transformed to computational coordinates:

$$\text{Irradiated surface, } \zeta = 1 : \quad \alpha \mathbf{Q} \cdot \nabla\zeta = -N_k^* \left[ A^{\xi\xi}\theta_\xi + A^{\eta\zeta}\theta_\eta + A^{\zeta\zeta}\theta_\zeta + \zeta_t \text{Ste}^* \right] \quad (13)$$

The other transformed boundary conditions are:

$$\text{Far upstream, } \xi = 1 : \quad \theta = 0 \quad (14a)$$

$$\text{Far sideways, } \eta = N_\eta : \quad \theta = 0 \quad (14b)$$

$$\text{Far downstream, } \xi = N_\xi : \quad \theta_x = \xi_x\theta_\xi + \eta_x\theta_\eta + \zeta_x\theta_\zeta = 0 \quad (14c)$$

$$\text{In the center plane, } \eta = 1 : \quad \theta_y = \xi_y\theta_\xi + \eta_y\theta_\eta + \zeta_y\theta_\zeta = 0 \quad (14d)$$

The evaporating condition becomes:

$$\zeta = 1 : \quad \zeta_t = -\frac{V_n}{|\nabla\zeta|} = -\frac{C_1}{|\nabla\zeta|} e^{C_2[1-T_{re}/T(\theta)]} \quad (15)$$

Equation (14c) is used instead of a constant ambient temperature boundary condition,  $\theta = 0$ , since the grid is truncated at a finite distance downstream of the laser heating zone. However, the boundary surface,  $\xi = N_\xi$ , is constructed far enough from the evaporating groove surface such that  $\theta$  is very small.

### 3.3 Grid Generation

A computational coordinate system was constructed with  $N_\xi \times N_\eta \times N_\zeta$  nodal points in the region bounded by the irradiated surface, ( $\zeta = 1$ ) and another surface ( $\zeta = N_\zeta$ ), “far” away into the body not heated by the laser. As the laser moves across the surface different parts of the workpiece become heated by the laser beam. Thus, nodes are continuously added ahead of the laser beam and dropped in its rear. It is desirable to maintain uniform nodal spacing of  $\Delta\xi = \Delta\eta = \Delta\zeta = 1$

between the nodal points, which simplifies difference representation in computational space. The present study is limited to the case where the absorbed irradiation is symmetric about the center plane resulting in a symmetric groove. Therefore, the grid is constructed on one side of the center plane. In Fig. 2 the computational domain  $(\xi, \eta, \zeta)$ , which is a rectangular parallelepiped is shown alongside the physical domain  $(x, y, z)$  bounded by curved surfaces.

A number of considerations are important for the construction of the computational nodal system:

1. The nodes must be smoothly distributed across the computational domain; nodes may not be spaced apart too much wherever substantial temperature gradients are expected.
2. The grid system needs to be self-adaptive, automatically deforming itself as the laser removes and shapes material.
3. Because of the rapid recession and deformation of the computational domain the nodal network needs to be recalculated during each time step; therefore, the nodal network construction must be very simple to allow rapid recalculation.

These above considerations make the construction of a three-dimensional grid system a formidable problem! Thankfully, the problem is somewhat simplified by the fact that the heat-affected zone is usually only a thin surface layer, ranging in thickness from 1 to 2 laser radii for CW laser operation to as little as 0.1 radii and less for pulsed operation. Thus, the problem may be broken up into two parts: (i) generation of the nodal network on the top (irradiated surface), and (ii) calculation of internal nodes. Computational efficiency dictates that all grid generation needs to be done using simple algebraic interpolation functions.

Surface nodes The projection of the top surface of the computational zone is assumed to be rectangular. A simple hole drilled into the workpiece would produce a deep, circular indentation in a rectangular body. All two-dimensional methods to produce a “good” network on such a system as described by Thompson *et al.* [22] were tried and failed, since a) they have difficulty accomodating a circular shape within a rectangular frame, and b) they have great difficulty placing regular nodes on the sharp apex of a deep hole. O- and C-grids [24] would be expected to cope better with the circular indentation; however, this approach would make it difficult to add and drop nodes as the laser scans across the surface (and, in future extensions of the model, to accomodate overlapped grooves and other shaping operations). On the other hand, for the vast majority of problems it is quite acceptable to use constant spacing in the  $x$ - and  $y$ -directions ( $\Delta x = \text{const}$ ,

$\Delta y = \text{const}$ ): grid spacing tends to get large only on very steep surfaces; these steep surfaces, however, tend to be almost isothermal (since ablation is taking place on their surface) without substantial conduction along them, or they are far away from the laser-interaction zone (*i.e.*, they are unimportant). Exceptions to this rule are cases with strong internal reflections and/or a strongly diverging laser beam focused inside the workpiece: in both cases the sidewalls may become **very** steep or even fold back (*i.e.*, the width of the groove inside the solid may be larger than near the surface). We will limit ourselves here to constant spacing in the  $x$ - and  $y$ -directions.

Internal Nodes Once the surface nodes have been established, the internal grid points for each surface node need to be generated. Lines of ( $\xi = \text{const}$ ,  $\eta = \text{const}$ ) need to move smoothly from the surface ( $\zeta = 1$ ) to a point “far” inside the material ( $\zeta = N_\zeta$ ); the various lines may not interfere with one another, indeed, they should stay as far apart as possible everywhere to minimize numerical instability. Near the surface (where the largest temperature gradients are) the lines need to be perpendicular to the surface (to minimize truncation error [22]). Therefore, the internal nodal system is designed such that the local unit tangent to a ( $\xi = \text{const}$ ,  $\eta = \text{const}$ ) line is given by (see Fig. 3)

$$\hat{\mathbf{t}} = c_\nu \hat{\mathbf{n}} + p_\nu \hat{\mathbf{s}}_\ell, \quad (16)$$

where

$$\begin{aligned} c_\nu &= (1 - \nu)^{C_k}, \\ p_\nu &= \sqrt{c_\nu^2 (\hat{\mathbf{n}} \cdot \hat{\mathbf{s}}_\ell)^2 + 1 - c_\nu^2} - c_\nu (\hat{\mathbf{n}} \cdot \hat{\mathbf{s}}_\ell), \\ \nu &= \frac{\zeta - 1}{N_\zeta - 1}. \end{aligned} \quad (17)$$

Here  $\hat{\mathbf{s}}_\ell$  is the desired gridline direction at the “far-inside” point ( $\nu = 1$ );  $c_\nu$  has been chosen such that  $\hat{\mathbf{t}} = \hat{\mathbf{n}}$  at the surface, and such that the morphing of  $\hat{\mathbf{n}}$  towards  $\hat{\mathbf{s}}_\ell$  can be controlled by  $\partial c_\nu / \partial \nu (\nu = 0) = -C_k$ . The value for  $p_\nu$  follows from  $c_\nu$  if  $\hat{\mathbf{t}}$  is to be a unit vector. Finally,  $\hat{\mathbf{s}}_\ell$  is chosen to be a weighted average of surrounding surface normals and a forcing function, which bends  $\hat{\mathbf{s}}_\ell$  toward the  $z$ -direction, *i.e.*,  $\hat{\mathbf{k}}$  (sometimes helpful, if geometry is **extremely** warped).

Along the grid lines grid points need to be placed at proper intervals: (a) the grid points should be spaced such that temperature differences from point to point are roughly equal, (b) grid point distance should vary smoothly to minimize truncation error. Thus, many grid points need to be placed near the surface (with its strong temperature gradients), and the spacing needs to gradually

open up for larger  $\zeta$ . Consequently, the following spacing scheme has been implemented:

$$s_k = \frac{\nu(1 + A\nu^2)}{1 + A}D, \quad (18)$$

where  $s_k$  is the arc length along the gridline ( $\xi = \text{const}$ ,  $\eta = \text{const}$ ) from the surface ( $\zeta = 1$ ) to point  $k$  ( $\zeta = k$ ), and  $D$  is the total arc length thickness of the heat-affected zone (input by the user). Equation (18) has a linear and a cubic component: near the surface ( $\zeta$ ,  $\nu$  small) the spacing is almost linear, resulting in equally-spaced nodes (and low truncation error), fanning out rapidly for larger values of  $\zeta$ . The value of  $A$  determines how closely the nodes are spaced near the surface, and is chosen such that the temperature difference between the surface and the first inside node is roughly  $\theta_{i,j,1}/(N_\zeta - 1)$  (*i.e.*, aiming for equal  $\Delta\theta$  between all grid points) although, for numerical stability,  $s_2$  is not allowed to become smaller than a specified minimum value ( $s_2 \geq s_{2,\min}$ ). Therefore, the grid spacing is automatically adjusted locally, placing many nodes near those parts of the surface where the heat-affected layer is thin, and spreading them out where the heat-affected layer is thicker.

## 4 Computational Procedure

The transformed equation (12) in  $\theta$  is finite-differenced and solved using a semi-implicit algorithm. In this scheme  $\theta_\zeta$  and  $\theta_{\zeta\zeta}$  are finite-differenced implicitly (*i.e.*, evaluated at time step  $\tau + \Delta\tau$ ) and the non-linear ablation condition (15) is also evaluated at  $\tau + \Delta\tau$ ; all other  $\theta$ -derivatives are finite-differenced explicitly (*i.e.*, evaluated at time  $\tau$ ). The reasoning is as follows: the stability of an explicit scheme is governed by two factors. The first is the magnitude of  $\Delta\tau/\Delta s^2$  (where  $\Delta\tau$  is the time step and  $\Delta s$  is the smallest distance between two nodes); the second is the nonlinearity of the ablation condition. Normal to the ablating surface (*i.e.*, into the  $\zeta$ -direction) the temperature drops very rapidly necessitating very small nodal steps in that direction ( $\Delta s$  as small as  $10^{-4}$ ). Therefore, unless meaninglessly small time steps are considered, finite-differencing needs to be implicit in  $\zeta$ . The cross-derivative terms will always be small since, near the top surface,  $\zeta$  is orthogonal to  $\xi$  and  $\eta$  (making  $A^{\xi\zeta} \simeq A^{\eta\zeta} \simeq 0$ ), and far away from the top  $\theta$  is small. Evaluation of the ablation condition also must be implicit: inspection of equation (15) shows it to be extremely sensitive to temperature near  $T = T_{re}$ , rapidly shooting from  $V_n \simeq 0$  to  $V_n \gg 1$ . Using this condition explicitly (*i.e.*, extrapolating it) would require very small changes in temperature and, therefore, too small time steps. The situation is quite different for  $\xi$ - and

$\eta$ -derivatives. In the planes  $\zeta=\text{const}$  nodal spacing is relatively large ( $\Delta s \simeq 0.02\text{-}0.2$ ). [Note that this may lead to very large values of  $(\Delta s_{\xi,\eta})_{\text{max}}/(\Delta s_{\zeta})_{\text{min}}$ ; to maintain a stable finite difference scheme, values of  $(\Delta s_{\xi,\eta})_{\text{max}}/(\Delta s_{\zeta})_{\text{min}} \gg 1$  should be avoided]. Typical non-dimensional times required to heat a solid with a laser from room temperature to the ablation point range from  $10^{-4}$  (CW) to  $10^{-6}$  (Q-switched pulse); choosing time steps of that magnitude or smaller would be typical. Therefore, violation of the stability condition for explicit calculations,  $\Delta\tau/\Delta s^2 < 0.5$ , appears very unlikely, and nothing would be gained from using an implicit scheme. Consequently, the second-order-accurate finite differences for first, second and mixed derivatives are represented as:

$$\delta_{\xi}(\theta)_{i,j,k}^n = \frac{1}{2}(\theta_{i+1,j,k}^n - \theta_{i-1,j,k}^n) \quad (19a)$$

$$\delta_{\xi\xi}(\theta)_{i,j,k}^n = \theta_{i+1,j,k}^n + \theta_{i-1,j,k}^n - 2\theta_{i,j,k}^n \quad (19b)$$

$$\delta_{\eta\xi}(\theta)_{i,j,k}^n = \frac{1}{4}[(\theta_{i+1,j+1,k}^n - \theta_{i-1,j+1,k}^n) - (\theta_{i+1,j-1,k}^n - \theta_{i-1,j-1,k}^n)] \quad (19c)$$

$$\delta_{\zeta}(\theta)_{i,j,k}^{n+1} = \frac{1}{2}(\theta_{i,j,k+1}^{n+1} - \theta_{i,j,k-1}^{n+1}), \quad (19d)$$

etc., where  $i, j, k$  represent grid point indices and  $\delta_{\xi}, \delta_{\eta}, \delta_{\zeta}$  represent finite differencing in  $\xi, \eta, \zeta$  directions, respectively.

At the boundary points where, at most, first-order partials must be represented, a second-order accurate one-sided difference was used to approximate  $\theta_{\zeta}$ . The second order formula appropriate for the boundary point  $(i, j, 1)$  on the surface  $\zeta = 1$  is:

$$\delta_{\zeta}(\theta)_{i,j,1}^{n+1} = \frac{1}{2}(-\theta_{i,j,3}^{n+1} + 4\theta_{i,j,2}^{n+1} - 3\theta_{i,j,1}^{n+1}) \quad (20)$$

Second-order differencing must be used at the groove boundary,  $\zeta = 1$ , because the temperature change can be very high into the body over the nodes even though the nodes are placed closely. However, one-sided differencing of the coordinate values in the  $\zeta$ -direction, *e.g.*,  $x_{\zeta}$ , need only be first-order accurate because the nodes are closely spaced.

The governing equation is then represented in difference form as:

$$\frac{1}{f^{n+1}} \left[ \frac{\theta^{n+1}}{\Delta\tau} + \zeta_t \delta_{\zeta}(\theta^{n+1}) \right] - A^{\zeta\zeta} \delta_{\zeta\zeta}(\theta^{n+1}) - \nabla^2 \zeta \delta_{\zeta}(\theta^{n+1}) =$$

$$\frac{1}{f^{n+1}} \left[ \frac{\theta^n}{\Delta\tau} - \xi_t \delta_{\xi}(\theta^n) - \eta_t \delta_{\eta}(\theta^n) \right] + \delta_{\xi}(\theta^n) \nabla^2 \xi + \delta_{\eta}(\theta^n) \nabla^2 \eta$$

$$+ A^{\xi\xi}\delta_{\xi\xi}(\theta^n) + A^{\eta\eta}\delta_{\eta\eta}(\theta^n) + 2A^{\xi\eta}\delta_{\xi\eta}(\theta^n) + 2A^{\xi\zeta}\delta_{\xi\zeta}(\theta^n) + 2A^{\eta\zeta}\delta_{\eta\zeta}(\theta^n). \quad (21)$$

Similarly, the irradiated-surface condition becomes

$$A^{\zeta\zeta}\delta_{\zeta\zeta}(\theta^{n+1}) = -\frac{\alpha}{N_k^*}\mathbf{Q} \cdot \nabla\zeta - A^{\xi\xi}\delta_{\xi\xi}(\theta^n) - A^{\eta\eta}\delta_{\eta\eta}(\theta^n) - \zeta_t\text{Ste}^*, \quad (22)$$

with  $\zeta_t$  evaluated from the ablation condition (15). In equations (21) and (22) the variable-property function  $f$  is determined implicitly at time step  $n+1$  (for stability) while all metric coefficients are evaluated explicitly, at time step  $n$ .  $\zeta_t$  depends on  $\theta_{i,j,1}^{n+1}$  through the ablation condition and is, thus, also implicit. Nodal movement is evaluated from equation (11). In the simplest case, chosen here, the  $x$ - and  $y$ -coordinates of the top surface nodes remain fixed so that

$$(z_\tau)_{i,j,1} = -\zeta_t/\zeta_z, \quad (23a)$$

$$(\xi_t)_{i,j,1} = -z_\tau\xi_z = \xi_z\zeta_t/\zeta_z, \quad (23b)$$

$$(\eta_t)_{i,j,1} = -z_\tau\eta_z = \eta_z\zeta_t/\zeta_z, \quad (23c)$$

The  $\xi_t$ ,  $\eta_t$  and  $\zeta_t$  for internal nodes (and their corresponding new  $x$ ,  $y$ ,  $z$ -coordinates) are found from the grid generation scheme described in the previous section.

Equations (21) and (22) give rise to tridiagonal matrices for each  $\xi$ ,  $\eta$  location. The algorithm, therefore, requires a series of scalar, tridiagonal inversions and can be solved efficiently, although iterations are required because of the nonlinearity of equation (15). In the iterative procedure the correct value for  $\theta_{i,j,1}^{n+1}$  is obtained by first bracketing it: a negligible value for  $V_n$  would require a minimum value for  $\theta_{i,j,1}^{n+1}$ , while assuming zero conduction losses in equation (13) yields a maximum value. The correct root is then found by Ridder's method [Numerical Recipes, [25], after slight modification necessitated by the strong nonlinearity of equation (15)]. Since only a single sweep over all  $\xi$ ,  $\eta$  locations (with a tridiagonal inversion for the  $\zeta$ -direction) is required for each time step, the method is roughly three times as efficient as the scheme of Roy and Modest [13] (but of similar accuracy).

## 5 Numerical Accuracy and Model Validation

The numerical accuracy of the model was validated by comparing its results with those of Roy and Modest [13] for constant and variable property, quasi-steady test cases. Results for groove shape and depth were virtually identical, except that for small velocities ( $U = 2$ ) small deviations ( $< 5\%$

for predicted groove depths) were observed. Numerical experiments indicated that the solution is extremely sensitive to nodal spacing in the  $\zeta$ -direction whenever conduction losses are substantial (small  $U$ ). Roy and Modest's [13] code used equal  $\zeta$ -spacing for all  $\xi, \eta$ -locations; since at the bottom of the groove the thermal penetration layer is extremely thin, their nodal spacing near the bottom surface was too far apart, resulting in underpredicted conduction losses and overpredicted groove depths. The present code automatically places nodes close together where the penetration layer is thin, and spaces them far apart where the layer is thicker. Numerical experiments also showed that, once a small enough value for  $s_{2,\min}$  has been identified, the results are of sufficient accuracy if  $N_\zeta \simeq 16$  to 20 (*i.e.*, further increases in  $N_\zeta$  change the groove shape by less than 1%).

Nodal movement into the  $\zeta$ -direction (for each time step) was of some concern: since nodal spacing near the surface is often so small, keeping nodal movement (due to the movement of the ablation front) below  $\zeta_t = \Delta\zeta/\Delta\tau < 1$  (*i.e.*, the new location  $\mathbf{r}_{i,j,1}^{n-1}$  does not move beyond the old subsurface location  $\mathbf{r}_{i,j,2}^n$ ) would require very small timesteps. Numerical experiments showed that values as large as  $|\zeta_t| = 500$  had no detrimental effects (by comparing with results obtained with a  $\Delta\tau$  small enough to keep  $|\zeta_t| < 1$ ); this is apparently due to the fact that all  $\zeta$ -nodes move together, and the *relative* movement between them is small.

Finally, decreasing the size of  $\Delta x$  and  $\Delta y$  showed that values of  $(\Delta s_{\xi,\eta})_{\max}/(\Delta s_\zeta)_{\min} = 1000$  and larger have no negative effects on the solution.

## 6 Sample Results and Discussion

The governing equation (8) and its auxiliary conditions (9) contain a large number of non-dimensional parameters ( $U, N_k, Ste, z_0, \beta_\infty, t_p$ , and, for the ablation condition,  $C_1, C_2, T_{re}$ ) making exhaustive presentation of the various parameters' influence on laser machining on a few pages impossible. The situation is aggravated by the fact that the temporal pulse variation,  $\phi(t)$ , will vary from laser to laser, and the dependence of  $f$  and  $\alpha$  on temperature (and, in the latter case, on laser incidence direction) varies from material to material. Therefore, we will limit the discussion here to a single "typical" set of laser and material parameters, investigating turn-on and turn-off effects, and comparing the performance of CW, long-pulsed (10% laser-on fraction) and rapidly-pulsed (0.1% laser-on fraction) lasers, using step function pulses. Variable property effects and the influence of pulse rise and decay effects will be discussed in a follow-up paper, which will deal exclusively with comparing the present model's results with experiment. Such comparisons have

been made for quasi-steady CW operation on silicon nitride (Roy and Modest [13]), and a few CW experiments on graphite have been presented in a companion paper by Modest et al. [26], which deals with the extension of the present model to predict laser entry and exit effects, as well as the shapes of overlapping grooves. Very good qualitative agreement between model and experiment was found.

In all the following figures, most parameters were kept at fixed values; *viz.*,  $Ste = 2.5$  (typical value for ceramics),  $z_o = 0$  (laser focused on surface),  $\beta_\infty = 0.02$  (average beam quality),  $U = 1$  and  $N_k = 0.05$  (equal scanning speed and total energy deposition per unit area);  $C_1 = 10$ ,  $C_2 = 100$  (assuring that ablation is limited to a very small temperature range around  $\theta \simeq 1$ ),  $\alpha = 0.9$  (highly absorbing material to avoid multiple-reflection effects in deep grooves), and  $f = \lambda_k = 1$  (constant properties). For pulsed operation it was assumed that, at the beginning of the pulse, pulse power would jump instantaneously to a constant maximum power and would drop instantaneously back to zero power after an on-time of  $t_{p,on}$ .

For pulsed laser operation pulse periods of  $t_p = 0.5, 0.75$  and  $1.0$  were chosen: for a non-dimensional scanning speed of  $U = 1$  this implies that the laser advances precisely  $t_p$  beam radii between two pulses, allowing us to study pulse overlap effects on groove surface smoothness. For the rapidly pulsed laser the laser-on time was taken as  $10^{-3}t_p$ : this scenario may be thought of as a Q-switched Nd:YAG laser processing a ceramic at a 10 kHz pulse rate, with an average power of  $\sim 30$  W and a scanning velocity of  $\sim 10$  cm/s. For the normally-pulsed laser the laser-on time was taken as  $0.1t_p$ : this may be thought of as a regularly pulsed Nd:YAG laser with a pulse rate of 1 kHz (laser-on time  $100\mu s$ ), a laser radius of  $75\mu m$ , scanning at 3 cm/s with an average power of 100 W; or it could be a 250 W average power CO<sub>2</sub> laser with a  $200\mu m$  beam radius, scanning at 2 cm/s while pulsing at a rate of 100 Hz (laser-on time of 1 ms). By the same token the CW case may be thought of as the same Nd:YAG or CO<sub>2</sub> laser running in CW mode. Note that, for otherwise equal conditions, the regularly-pulsed lasers have 10 times the CW power for the duration of the pulse, while the Q-switched laser packs 1000 times the CW power (during its 0.1% on-time).

Figure 4a compares the groove depths along the centerline ( $y = 0$ ) for different pulsing conditions. In all cases the laser is turned on when the laser center is at location  $x = 5, y = 0$ , and is turned off again after completion of the first pulse that carries the laser beyond  $x = 9, y = 0$  (i.e., after 9 pulses for  $t_p = 0.5$ ; 6 pulses for  $t_p = 0.7$ ; and 5 pulses for  $t_p = 1.0$ ). This implies that the  $t_p = 0.5$  and  $t_p = 0.75$  cases received an equal total amount of energy (the equivalent of 9  $t_p = 0.5$  pulses), while the  $t_p = 1.0$  case received a little more (5 double pulses or 10  $t_p = 0.5$  equivalents),

making its groove a little longer, and the CW case received a little less (the equivalent of  $8 t_p = 0.5$  pulses). For the Q-switched laser forward movement of  $0.5w_o$  and even  $0.75w_o$  between pulses results in a smooth bottom surface, while for a normally-pulsed laser even at a forward movement of  $0.5w_o$  some wiggles appear. This is due to the fact that the Q-switched laser has a larger effective ablation area, as will be seen in later figures. Comparing Q-switched, regularly-pulsed and CW operation reveals that conduction losses are virtually negligible for Q-switched operation, small for a regularly-pulsed laser (resulting in a slightly less deep groove), and very substantial for the CW laser. This is also the reason that, at laser turn-on, the groove wall is much less steep for the CW laser than it is at laser turn-off (since much surrounding material must be preheated). One additional curve has been included for a Q-switched laser with  $t_p = 0.5$  and a higher scan velocity  $U = 1.5$  (also advancing  $0.75w_o$  between pulses). This line shows that no advantage is gained by minimizing pulse overlap: this scenario receives  $2/3$  the energy of the  $t_p = 0.5, U = 1$  case resulting in  $\sim 2/3$  of the material removal rate.

Figure 4b shows cross-sections for the same grooves, each taken at their greatest depth. Similar to the centerline cut it is observed that the Q-switched laser makes the widest, steepest groove, and the CW laser the narrowest grooves.

Typical temperature rise and fall profiles shortly after the beginning and the end of a laser pulse, respectively, are shown in Figs. 5 through 10. Figure 5 depicts how the material heats up at the beginning of a Q-switched laser pulse. After a single timestep of  $\Delta\tau = 10^{-7}$  (corresponding to  $\simeq 20$ ps) a substantial part of the groove surface has reached ablation temperature, and after a time of only  $5 \times 10^{-6}$  ( $\simeq 1$ ns) covers about half of the eventual ablation zone as seen by comparing with the first frame of Fig. 7 [results from these figures should be taken as qualitative since (i) jumping from ambient to ablation temperature in a single time step is bound to be accompanied by large errors, and (ii) at time scales of 20 ps the use of Fourier's law of heat conduction becomes questionable]. Note that the distance over which the surface temperature drops from ablation temperature to near-ambient conditions is very small (about a quarter beam radius). The heat-affected layer inside the material is also extremely thin during the entire pulse, especially where ablation is taking place: the ablation front almost catches up with the diffusion front (Fig. 6); only along the bottom tail of the groove (Fig. 6b) as well as along its rim (Fig. 6a) does heat penetrate appreciably into the medium, but still less than  $0.1 w_o$ . Figure 7 demonstrates how rapidly the material cools off at the end of a pulse, reaching near-ambient conditions at the bottom of the groove after a few nanoseconds (again, this is qualitative since real pulses tend to decay over tens

of nanoseconds). The rim remains hot for a considerably longer time: at the bottom of the groove heat can diffuse into cold material into almost all directions (concave surfaces), while at the rim heat from surrounding areas is diffusing into the same volume (convex surface) [again, results should be seen as qualitative, also since real pulses have pulse decay times, and since hot gases not considered in the model may convectively heat the surface].

Figures 8 through 10 show the corresponding behavior for the normally-pulsed case. The behavior is qualitatively similar, but heat-up and cool down are several orders of magnitude slower. The distance over which surface temperature drops is considerably larger ( $\simeq 0.5 w_0$ ), and the thickness of the heat-affected zone is one order of magnitude higher. Again, this zone is much thinner wherever ablation occurs and, after turning the laser off, the concave bottom cools much more rapidly than the convex rim.

Internal temperature profiles during CW scribing, as well as cool-down isotherms after turning the laser off, look quite similar to the normally-pulsed case, Figs. 9 and 10. The equivalent internal temperatures are shown in Fig. 11, showing a heat-affected zone that is about three times thicker ( $\sim 1.5 w_0$ ).

## 7 Conclusions

A three-dimensional, fully transient conduction model has been developed that is capable of predicting the shape of a developing hole or groove that is formed by ablation of material, caused by a stationary or moving laser. The model allows the treatment of variable thermophysical and radiative material properties, as well as laser intensities of arbitrary spatial and temporal shape. Sample calculations were carried out to study the qualitative differences in material removal when CW, normally-pulsed (pulse length  $\sim 100 \mu s$ ) and short-pulsed (pulse length  $\sim 100 ns$ ) lasers are employed. The results show that during short-pulsed laser ablation conduction losses are essentially negligible, resulting in substantially larger removal rates than for CW operation for otherwise identical conditions, and an extremely thin (small fraction of a single beam radius) heat-affected layer. Ablation with normally pulsed lasers, on the other hand, results in removal rates, which approach those of a Q-switched laser, but the thickness of the heat-affected layer is much larger, approaching that of the CW laser. The calculations further indicate that, during short-pulsed laser ablation, the material cools off rapidly after the end of the pulse, returning to ambient conditions well before the beginning of the subsequent pulse.

## Acknowledgment

This work was carried out while the author was on sabbatical leave at the Institut für Strahlwerkzeuge (IFSW), University of Stuttgart, Germany. Their partial support and the support of the SEW-EURODRIVE Foundation are gratefully acknowledged.

## References

1. F. W. Dabby and U.-C. Paek, High-Intensity Laser-Induced Vaporization and Explosion of Solid Material, *I.E.E.E. J. Quantum Electron.*, **QE-8**, 106–111 (1972).
2. R. E. Wagner, Laser Drilling Mechanics, *J. Appl. Phys.*, **45**, 4631–4637 (1974).
3. D. Schuöcker and W. Abel, Material Removal Mechanism of Laser Cutting, In *Proceedings of the SPIE*, (1983).
4. D. Petring, P. Abels, and E. Beyer, Werkstoffbearbeitung mit Laserstrahlung, *Feinwerktechnik and Messtechnik*, **96**, 364–372 (1988).
5. M. F. Modest and H. Abakians, Heat Conduction in a Moving Semi-Infinite Solid Subjected to Pulsed Laser Irradiation, *J. Heat Transfer*, **108**, 597–601 (1986).
6. M. F. Modest and H. Abakians, Evaporative Cutting of a Semi-Infinite Body With a Moving CW Laser, *J. Heat Transfer*, **108**, 602–607 (1986).
7. H. Abakians and M. F. Modest, Evaporative Cutting of a Semi-Transparent Body with a Moving CW Laser, *J. Heat Transfer*, **110**, 924–930 (1988).
8. S. Ramanathan and M. F. Modest, Effect of Variable Properties on Evaporative Cutting with a Moving CW Laser, In *Heat Transfer in Space Systems*, Vol. HTD–135, ASME, (1990).
9. S. Ramanathan and M. F. Modest, Single and Multiple Pass Cutting of Ceramics With a Moving CW Laser, In *Proceedings of the XXII ICHMT Intl. Symposium on Manufacturing and Materials Processing*, Dubrovnik, Yugoslavia, (1990).
10. S. Ramanathan and M. F. Modest, CW Laser Drilling of Composite Ceramics, In *Proceedings of ICALEO '91, Laser Materials Processing*, Vol. 74, San Jose, CA, 305–326 (1992).
11. S. Ramanathan and M. F. Modest, CW Laser Cutting of Composite Ceramics, In *Laser Advanced Materials Processing – LAMP '92*, Vol. 2, Nagaoka, Japan, 625–632 (1992).

12. S. Roy and M. F. Modest, Three-Dimensional Conduction Effects During Evaporative Scribing with a CW Laser, *J. Thermoph. Heat Transfer*, **4**(2), 199–203 (1990).
13. S. Roy and M. F. Modest, Evaporative Cutting with a Moving CW Laser — Part I: Effects of Three-Dimensional Conduction and Variable Properties, *Int. J. Heat Mass Transfer*, **36**(14), 3515–3528 (1993).
14. S. Y. Bang and M. F. Modest, Multiple Reflection Effects on Evaporative Cutting with a Moving CW Laser, *J. Heat Transfer*, **113**(3), 663–669 (1991).
15. S. Y. Bang, S. Roy, and M. F. Modest, CW Laser Machining of Hard Ceramics — Part II: Effects of Multiple Reflections, *Int. J. Heat Mass Transfer*, **36**(14), 3529–3540 (1993).
16. S. Y. Bang and M. F. Modest, Evaporative Scribing with a Moving CW Laser - Effects of Multiple Reflections and Beam Polarization, In *Proceedings of ICALEO '91, Laser Materials Processing*, Vol. 74, San Jose, CA, 288–304 (1992).
17. G. Chryssolouris, *Laser Machining: Theory and Practice*, Springer Verlag, New York, NY, 1st ed., (1991).
18. H. Kogelnik and T. Li, Laser Beams and Resonators, *Appl. Opt.*, **5**(10), 1550–1565 (1956).
19. J.T. Luxon and D.E. Parker, *Industrial Lasers and Their Applications*, Prentice-Hall, Englewood Cliffs, NJ, 1st ed., (1985).
20. P. S. Wei and J. Y. Ho, Energy Considerations in High-Energy Beam Drilling, *Int. J. Heat Mass Transfer*, **33**(10), 2207–2218 (1990).
21. H. S. Carslaw and J. C. Jaeger, *Conduction of Heat in Solids*, Oxford University Press, 2nd ed., (1959).
22. J. F. Thompson, Z. U. A. Warsi, and C. W. Mastin, *Numerical Grid Generation, Foundations and Applications*, North-Holland, New York, (1985).
23. D. A. Anderson, J. C. Tannehill, and R. H. Pletcher, *Computational Fluid Mechanics and Heat Transfer*, Hemisphere, New York, (1984).
24. R. E. Smith, Algebraic Grid Generation, In J. F. Thompson, ed., *Numerical Grid Generation*, Elsevier, 137–170 (1982).
25. W. H. Press, S. A. Teukolsky, W. T. Vetterling, and B.P. Flannery, *Numerical Recipes in FORTRAN – The Art of Scientific Computing*, Cambridge University Press, Cambridge, 2nd ed., (1992).

26. M. F. Modest, S. Ramanathan, A. Raiber, and B. Angstenberger, Laser Machining of Ablating Materials—Overlapped Grooves and Entrance/Exit Effects, In *Proceedings of ICALEO '94*, (1994).

## List of Figure Captions

Figure 1: Geometrical arrangement of laser and workpiece

Figure 2: Physical and computational grid systems.

Figure 3: Variation of the local unit tangent along a  $\xi=\text{const}$ ,  $\eta=\text{const}$  grid line.

Figure 4: Comparison of grooves generated with CW, pulsed and Q-switched lasers; (a) cross-sections along centerline, (b) cross-sections normal to laser scan direction.

Figure 5: Surface temperature development for small times after start of new pulse from short-pulsed laser ( $\tau_{p,\text{on}} = 0.0005$ ,  $\tau_p = 0.5$ ).

Figure 6: Internal temperature distributions at the end of a pulse from short-pulsed laser ( $\tau_{p,\text{on}} = 0.0005$ ,  $\tau_p = 0.5$ ); (a) cross-section transverse to laser movement, (b) cross-section along centerline.

Figure 7: Surface temperature development for small times after end of a pulse from short-pulsed laser ( $\tau_{p,\text{on}} = 0.0005$ ,  $\tau_p = 0.5$ ).

Figure 8: Surface temperature development for small times after start of new pulse from normal-pulsed laser ( $\tau_{p,\text{on}} = 0.05$ ,  $\tau_p = 0.5$ ).

Figure 9: Internal temperature distributions at the endpoint of a pulse from normal-pulsed laser ( $\tau_{p,\text{on}} = 0.05$ ,  $\tau_p = 0.5$ ); (a) cross-section transverse to laser movement, (b) cross-section along centerline.

Figure 10: Surface temperature development for small times after start of new pulse from normal-pulsed laser ( $\tau_{p,\text{on}} = 0.05$ ,  $\tau_p = 0.5$ ).

Figure 11: Internal temperature distributions resulting from a CW laser; (a) cross-section transverse to laser movement, (b) cross-section along centerline.

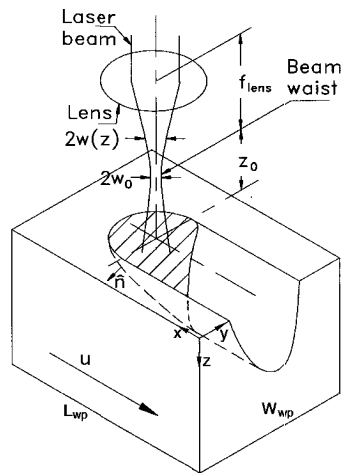


Figure 1: Geometrical arrangement of laser and workpiece

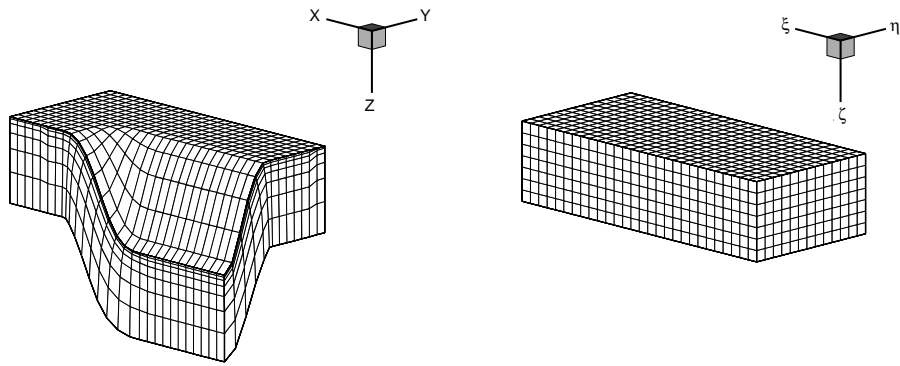


Figure 2: Physical and computational grid systems.

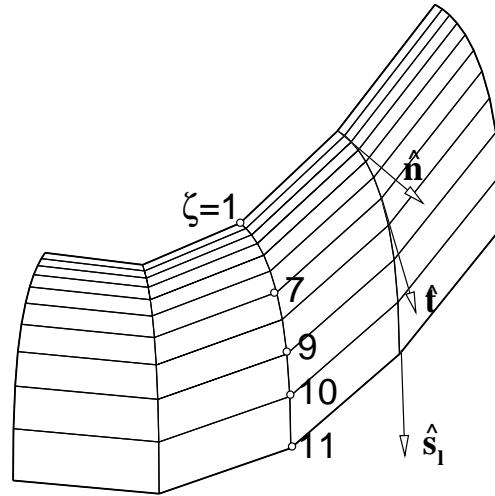


Figure 3: Variation of the local unit tangent along a  $\xi=\text{const}$ ,  $\eta=\text{const}$  grid line.

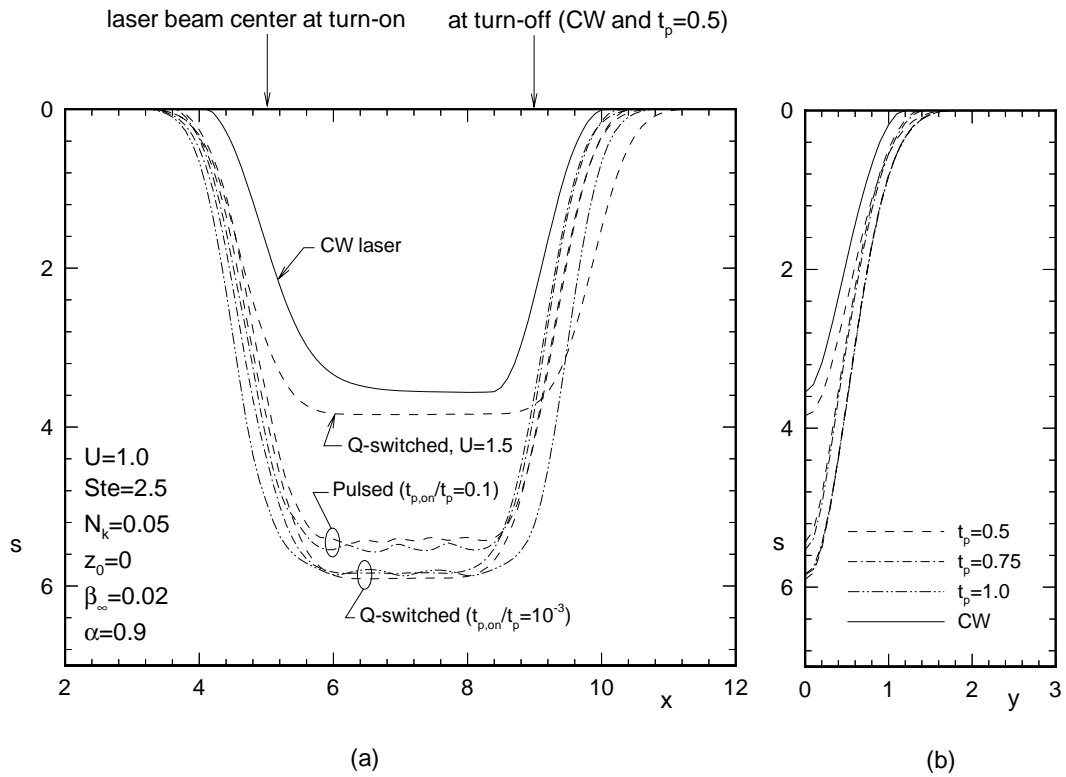
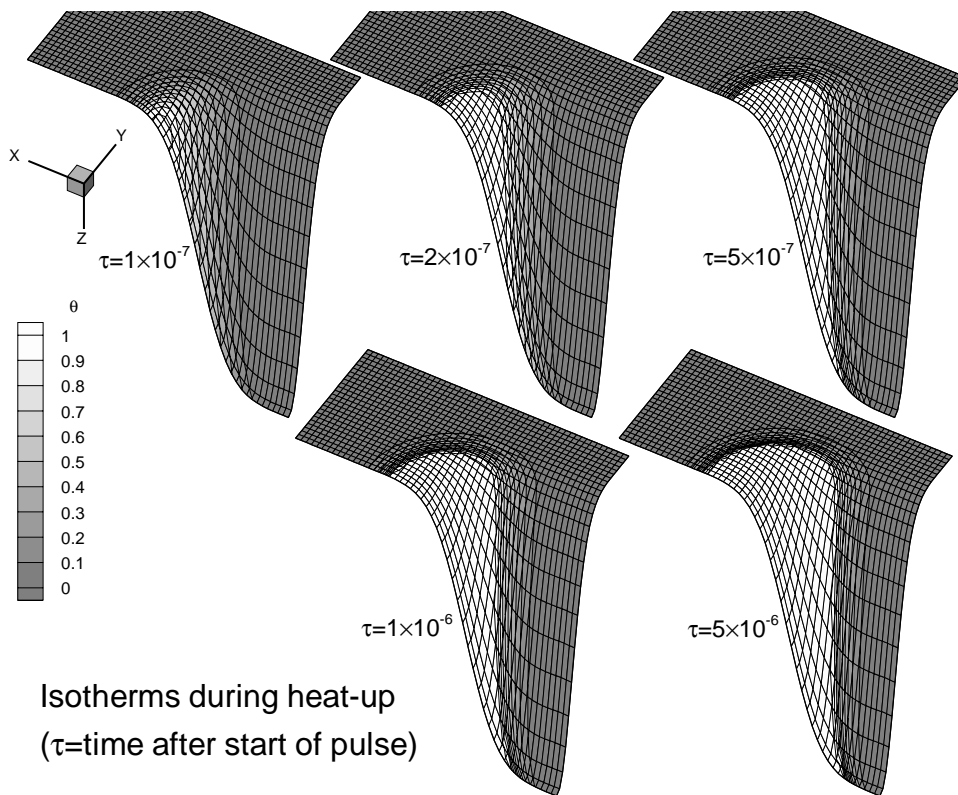


Figure 4: Comparison of grooves generated with CW, pulsed and Q-switched lasers; (a) cross-sections along centerline, (b) cross-sections normal to laser scan direction.



Isotherms during heat-up  
 ( $\tau$ =time after start of pulse)

Figure 5: Surface temperature development for small times after start of new pulse from short-pulsed laser ( $\tau_{p,on} = 0.0005$ ,  $\tau_p = 0.5$ ).

## Internal Temperature Distribution at End of Pulse

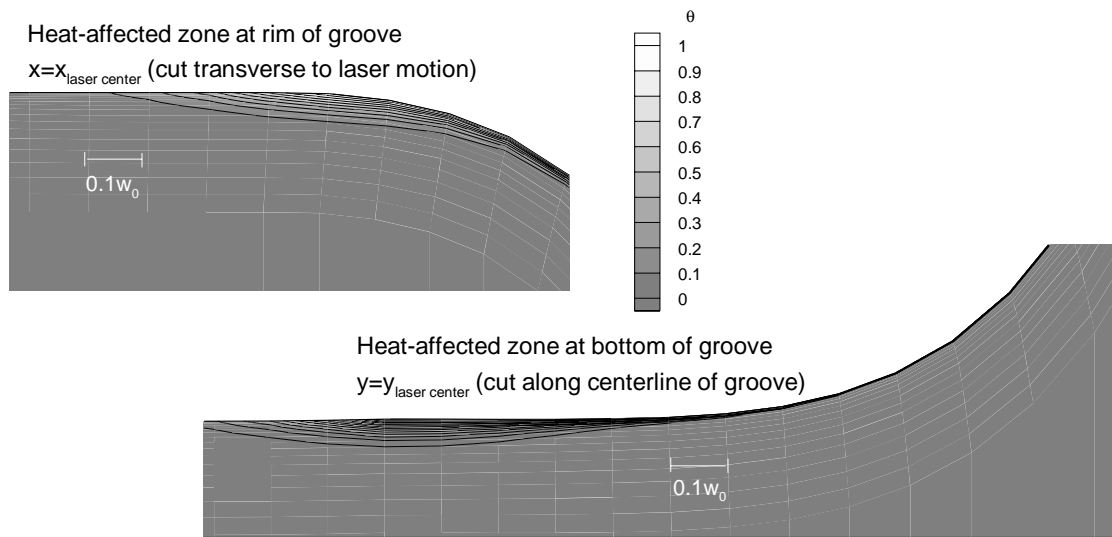


Figure 6: Internal temperature distributions at the end of a pulse from short-pulsed laser ( $\tau_{p,\text{on}} = 0.0005$ ,  $\tau_p = 0.5$ ); (a) cross-section transverse to laser movement, (b) cross-section along centerline.

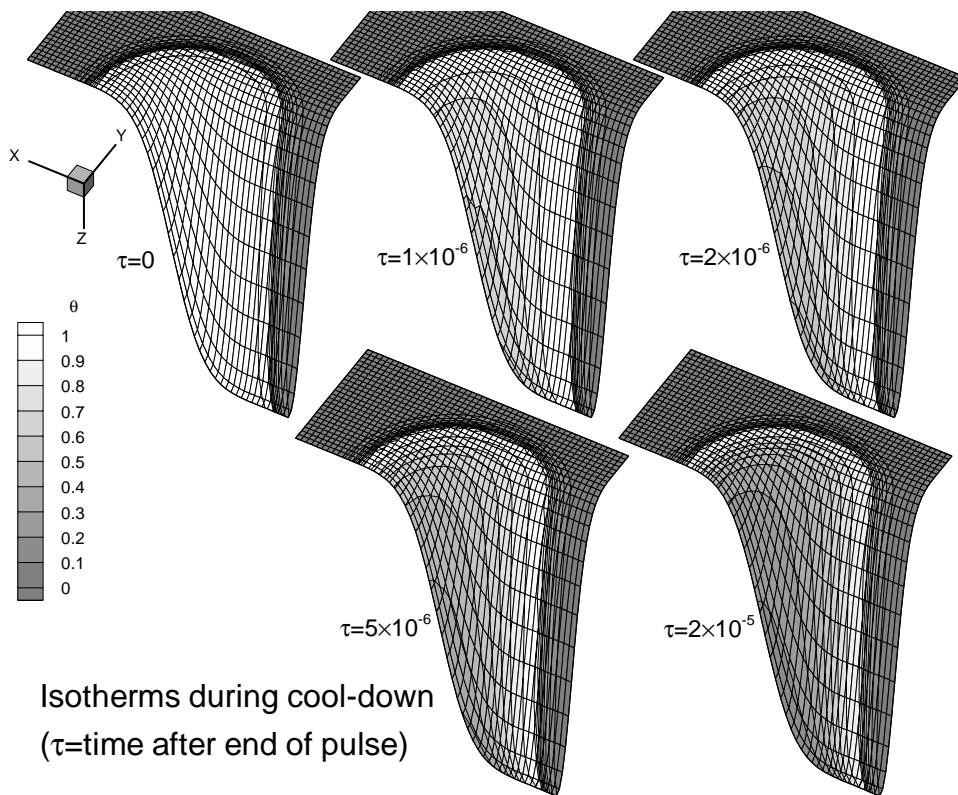
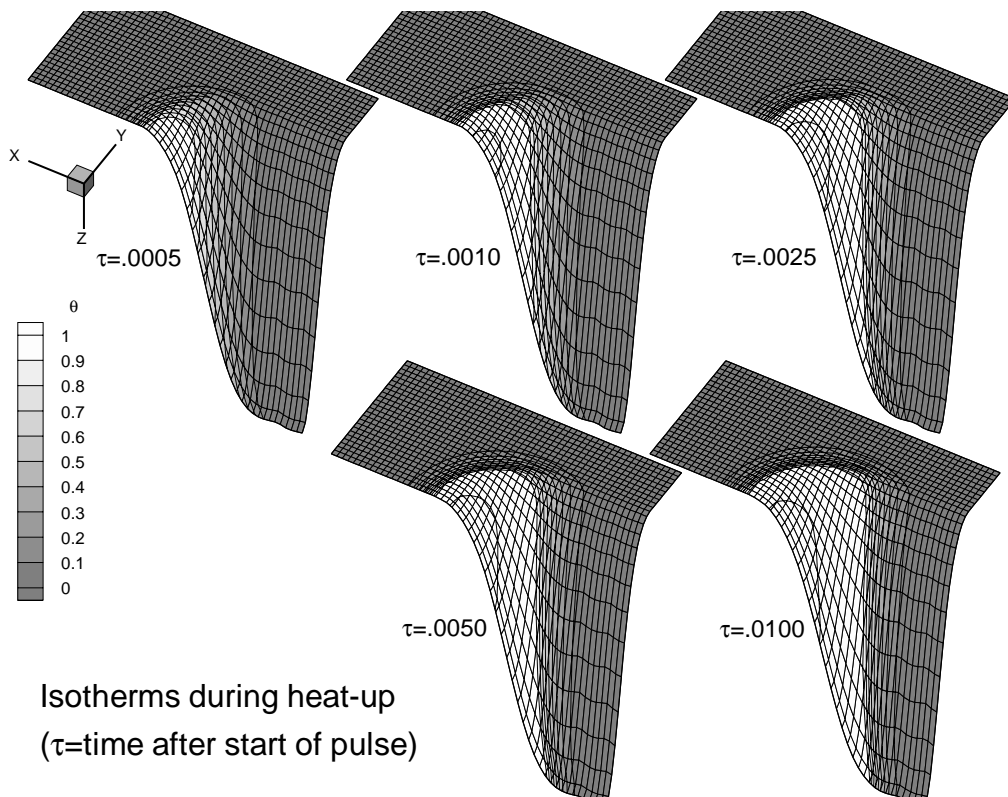


Figure 7: Surface temperature development for small times after end of a pulse from short-pulsed laser ( $\tau_{p,on} = 0.0005$ ,  $\tau_p = 0.5$ ).



Isotherms during heat-up  
 ( $\tau$ =time after start of pulse)

Figure 8: Surface temperature development for small times after start of new pulse from normal-pulsed laser ( $\tau_{p,on} = 0.05$ ,  $\tau_p = 0.5$ ).

### Internal Temperature Distribution for Pulsed Operation

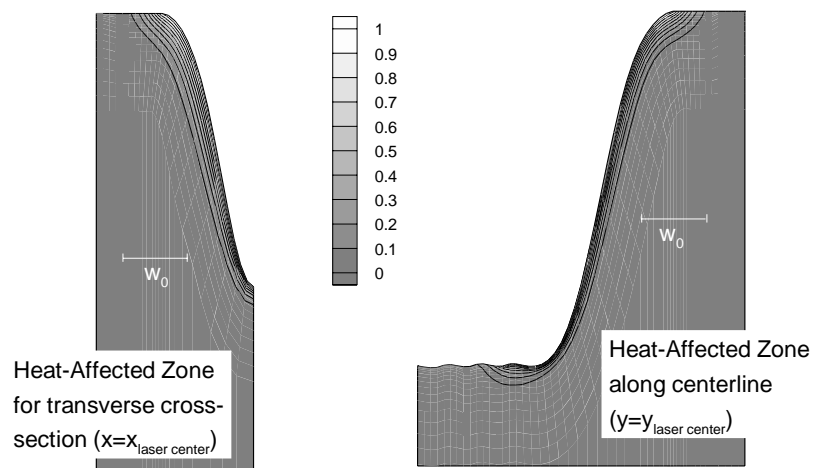


Figure 9: Internal temperature distributions at the endpoint of a pulse from normal-pulsed laser ( $\tau_{p,\text{on}} = 0.05$ ,  $\tau_p = 0.5$ ); (a) cross-section transverse to laser movement, (b) cross-section along centerline.

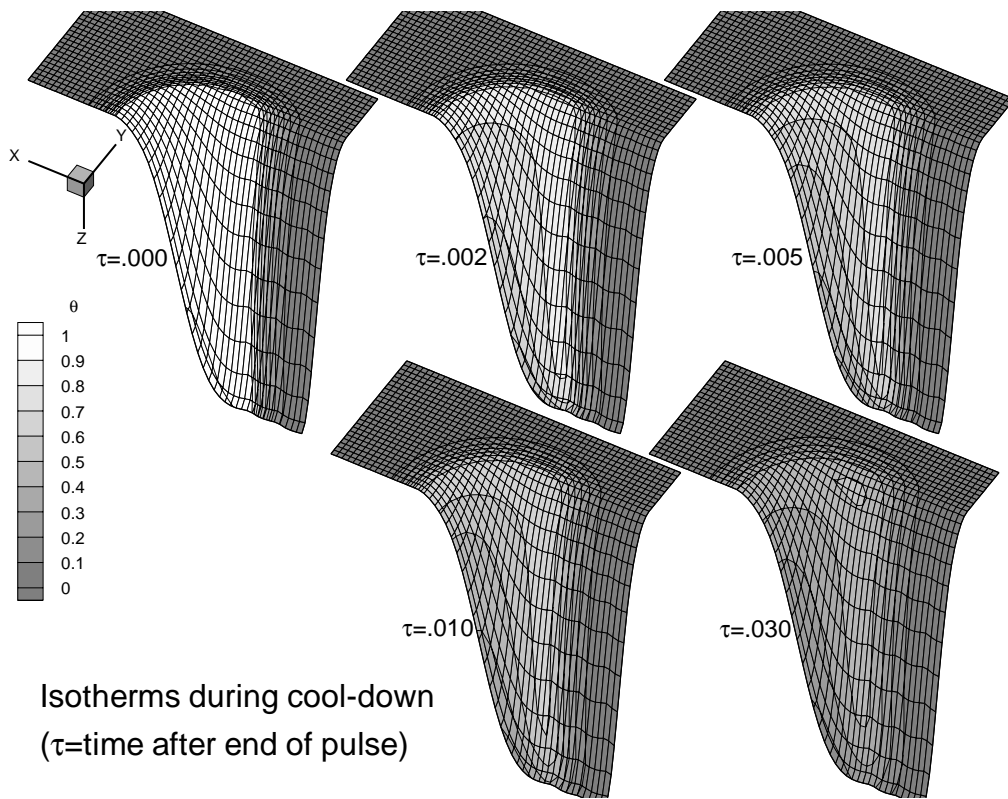


Figure 10: Surface temperature development for small times after start of new pulse from normal-pulsed laser ( $\tau_{p,on} = 0.05$ ,  $\tau_p = 0.5$ ).

### Internal Temperature Distribution for CW Operation

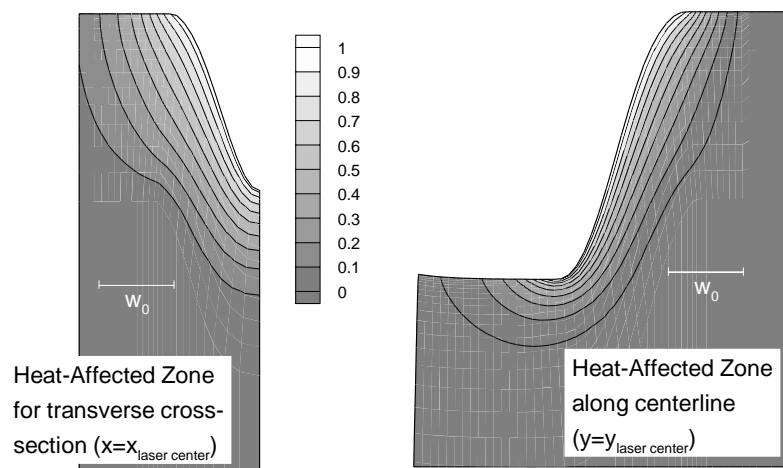


Figure 11: Internal temperature distributions resulting from a CW laser; (a) cross-section transverse to laser movement, (b) cross-section along centerline.